PAPER • OPEN ACCESS

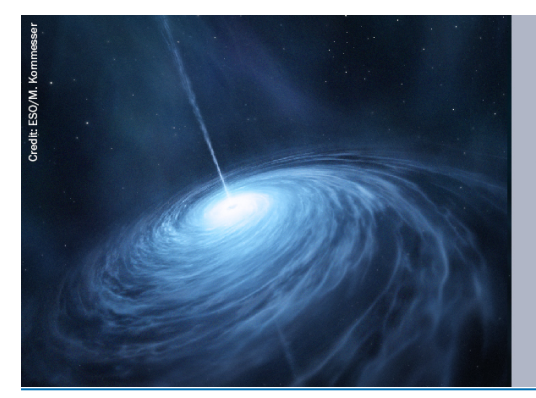
Global comparison of core-collapse supernova simulations in spherical symmetry

To cite this article: Evan O'Connor et al 2018 J. Phys. G: Nucl. Part. Phys. 45 104001

View the article online for updates and enhancements.

Recent citations

- <u>Neutrino Process in Core-collapse</u> <u>Supernovae with Neutrino Self-interaction</u> and MSW Effects Heamin Ko et al.
- Collective flavor conversion including the neutrino halo in core-collapse supernovae Masamichi Zaizen et al
- Constraining sterile neutrinos by corecollapse supernovae with multiple detectors
 Jian Tang et al







Start exploring the collection-download the first chapter of every title for free.



J. Phys. G: Nucl. Part. Phys. 45 (2018) 104001 (21pp)

Global comparison of core-collapse supernova simulations in spherical symmetry

Evan O'Connor^{1,2}, Robert Bollig^{3,4}, Adam Burrows⁵, Sean Couch^{6,7,8,9}, Tobias Fischer¹⁰, Hans-Thomas Janka³, Kei Kotake¹¹, Eric J Lentz^{12,13}, Matthias Liebendörfer¹⁴ O E Bronson Messer^{12,13,15}, Anthony Mezzacappa^{12,16}, Tomoya Takiwaki¹⁷ and David Vartanyan⁵

¹ Department of Astronomy and Oskar Klein Centre, Stockholm University, AlbaNova, SE-106 91 Stockholm, Sweden

² North Carolina State University, Department of Physics, Campus Code 8202, Raleigh, North Carolina, 27695, United States of America

³ Max-Planck-Institut für Astrophysik, Karl-Schwarzschild-Str. 1, D-85748 Garching, Germany

⁴ Physik Department, Technische Universität München, James-Franck-Straße 1, D-85748 Garching, Germany

⁵ Department of Astrophysical Sciences, Princeton University, Princeton, NJ 08544, United States of America

⁶ Department of Physics and Astronomy, Michigan State University, East Lansing, MI 48824, United States of America

⁷ Joint Institute for Nuclear Astrophysics-Center for the Evolution of the Elements, Michigan State University, East Lansing, MI 48824, United States of America

⁸ Department of Computational Mathematics, Science, and Engineering, Michigan State University, East Lansing, MI 48824, United States of America

⁹ National Superconducting Cyclotron Laboratory, Michigan State University, East Lansing, MI 48824, United States of America

¹⁰ Institute for Theoretical Physics, University of Wrocław, 50-204 Wrocław, Poland

¹¹ Department of Applied Physics, Fukuoka University, Nanakuma 8-19-1, Fukuoka 814-0180, Japan

¹²Department of Physics and Astronomy, University of Tennessee, Knoxville, TN 37996-1200, United States of America

¹³ Physics Division, Oak Ridge National Laboratory, PO Box 2008, Oak Ridge, TN 37831-6354, United States of America

¹⁴ Department für Physik, Universität Basel, CH-4056 Basel, Switzerland

¹⁵ National Center for Computational Sciences, Oak Ridge National Laboratory, PO Box 2008, Oak Ridge, TN 37831-6164, United States of America

E-mail: evan.oconnor@astro.su.se

Received 11 June 2018, revised 22 August 2018 Accepted for publication 4 September 2018 Published 14 September 2018



Abstract

We present a comparison between several simulation codes designed to study the core-collapse supernova mechanism. We pay close attention to controlling the initial conditions and input physics in order to ensure a meaningful and informative comparison. Our goal is three-fold. First, we aim to demonstrate the current level of agreement between various groups studying the corecollapse supernova central engine. Second, we desire to form a strong basis for future simulation codes and methods to compare to. Lastly, we want this work to be a stepping stone for future work exploring more complex simulations of core-collapse supernovae, i.e., simulations in multiple dimensions and simulations with modern neutrino and nuclear physics. We compare the early (first \sim 500 ms after core bounce) spherically-symmetric evolution of a 20 M_{\odot} progenitor star from six different core-collapse supernovae codes: 3DnSNe-IDSA, AGILE-BOLTZTRAN, FLASH, FORNAX, GR1D, and PRO-METHEUS-VERTEX. Given the diversity of neutrino transport and hydrodynamic methods employed, we find excellent agreement in many critical quantities, including the shock radius evolution and the amount of neutrino heating. Our results provide an excellent starting point from which to extend this comparison to higher dimensions and compare the development of hydrodynamic instabilities that are crucial to the supernova explosion mechanism, such as turbulence and convection.

Supplementary material for this article is available online

Keywords: core-collapse supernovae, neutrino transport, code comparison, neutron stars

(Some figures may appear in colour only in the online journal)

1. Introduction

Simulations of core-collapse supernovae have a long history, starting in the 1960s with the seminal work of [1–3]. Tremendous progress has been made since then. Today's simulations of core-collapse supernova are incredibly complex. Capturing all of the essential physics requires bringing together input microphysics from nuclear physics, neutrino physics, and

Original content from this work may be used under the terms of the Creative Commons Attribution 3.0 licence. Any further distribution of this work must maintain attribution to the author(s) and the title of the work, journal citation and DOI.

¹⁶ Joint Institute for Computational Sciences, Oak Ridge National Laboratory, PO Box 2008, Oak Ridge, TN 37831-6354, United States of America

¹⁷ National Astronomical Observatory of Japan, Mitaka, Tokyo 181-8588, Japan

stellar evolution, each of which remain uncertain to varying degrees, into multidimensional, general-relativistic, multi-species and multi-energy neutrino-radiation-magnetohydrodynamic simulations. Given the large multi-physics nature of these simulations, the large parameter space of initial conditions, and the varying abilities of individual simulation codes, comparisons between independent investigations have historically been difficult.

Many comparisons between different neutrino transport schemes have been made in the past. We briefly summarize some of these comparisons here. The first extensive comparisons were published in [4, 5], where multi-physics simulations of the infall phase using two codes, one employing Boltzmann neutrino transport and the other employing the multi-group fluxlimited diffusion solver of [6], were compared across a complete set of hydrodynamic, thermodynamic, and neutrino quantities. In [7], a detailed comparison of neutrino transport in static protoneutron star (PNS) atmospheres was done using both Monte Carlo and discreteordinate Boltzmann transport. There have also been comparisons, both in 1D [8] and 2D [9], where the focus was placed on comparing static postbounce snapshots of multi-group fluxlimited diffusion simulations with the solutions from Boltzmann neutrino transport solvers. [10] compare their variable Eddington factor (with a Boltzmann closure) method to various flux-limiting methods, and recently, [11] have compared 1D and 2D static configurations using Boltzmann transport and Monte Carlo transport and find excellent agreement. The most extensive comparison to date between two fully independent and dynamic calculations was presented in [12]. This work compared two codes, PROMETHEUS-VERTEX and AGILE-BOLTZTRAN (both are used in this comparison as well). Calculations were done both in Newtonian gravity and general-relativistic gravity, via spherically-symmetric simulations. While AGILE-BOLTZTRAN uses Boltzmann transport via the discrete-ordinate method, PROMETHEUS-VERTEX uses a two-moment scheme with a Boltzmann transport-derived closure. This seminal comparison has been extensively used in the literature as a basis for development of neutrino transport methods. Recently, [13] have done a comparison between two codes (PROMETHEUS-VERTEX and AENUS-ALCAR; in both 1D and 2D) using the initial conditions inspired by the work done here.

This article is an attempt to make a fair comparison between many of the core-collapse supernova simulation codes currently in use in the literature. Many comparisons that could be inferred from reviews of the literature, upon closer inspection, are not simulating the same problem. For example, in the two-dimensional works of [14–18], while many of the initial conditions are common, each set of neutrino physics is different in some way. This limits the interpretation of any comparison. Here, in this work, we focus on minimizing differences in the input physics so as to reduce potential sources of disparate results. To this end we use a basic set of neutrino opacities, do not include any nuclear burning, and restrict ourselves to spherical symmetry. In the future, comparisons built off this reference set are encouraged in order to examine more realistic scenarios, including multiple dimensions, nuclear burning, and modern opacities.

This comparison includes the following core-collapse supernova codes, each of which is described in detail below: 3DnSNe-IDSA, AGILE-BOLTZTRAN, FLASH, FORNAX, GR1D, and PROMETHEUS-VERTEX. Overall, we find excellent agreement between all of the codes. We typically see variations in the explored quantities that are ≤10%, and in some cases within a few % across all of the simulation codes. In particular, we see good agreement between highly nonlinear quantities, such as the neutrino heating and estimated neutrino detection rates, which depend sensitively on the neutrino spectra being emitted, and in the case of the neutrino heating, the hydrodynamic properties near the supernova shock. We do not attempt to describe or explain all of the differences we see, nor do we promote any particular code as more trustworthy than the others. In this article, we begin in section 2 by

describing the detailed initial conditions, neutrino physics, and non-neutrino physics of our comparison model. In section 3, we describe each of the different simulation codes used in this work. We pay special attention to note any differences from the prescribed plan of section 2. In section 4 we show the results of our comparison starting with hydrodynamic quantities, moving on to neutrino quantities and neutrino-matter coupling quantities. We end with comparison of estimated neutrino detection rates in Earth-based detectors. We summarize in section 5.

2. The setup

Here we describe, in detail, the initial conditions and the input physics used in this comparison. We split the description into two main parts, non-neutrino physics and neutrino physics. Any deviations from the details listed below by specific simulation groups are presented in the following section where the individual codes are described.

2.1. Non-neutrino physics

We utilize the $20 M_{\odot}$ (zero-age main sequence mass), solar metallicity, progenitor from [19]. We map the density, temperature, and electron fraction (Y_e) from the initial model to each simulation domain. We take the radial extent of the domain to be 10⁹ cm. For the sake of clarity, we note that the radial coordinate and the radial velocity in the progenitor model correspond to the value at the outer edge of the zone, while the remaining quantities are zone averages. We utilize the SFHo equation of state (EOS) [20]. This choice is motivated by the large range in density (down to $\sim 1600 \text{ g cm}^{-3}$) and temperature (down to 0.1 MeV) covered by the table that allows us to forgo any additional low-density or low-temperature treatment of the EOS and thereby removes a potential source of differences between simulation groups. This approach, which assumes nuclear statistical equilibrium (NSE) everywhere, inaccurately captures the composition and therefore the exact EOS in non-NSE regions of the progenitor star. However, it ensures consistency between the various simulations. Photons, electrons, and positrons are added to the baryonic EOS. The simulations are performed either with full general-relativistic (GR) gravity, or with an effective potential. For those simulations which utilize an effective potential, case A of [21] is used. For this initial work, we restrict ourselves to spherically symmetric simulations.

2.2. Neutrino physics

For the purposes of this comparison we use a simple, widely implemented, but outdated, set of neutrino opacities. For scattering and absorption on free nucleons we use the rates as presented in [6], and also implement weak magnetism and recoil corrections as described in [22]. For the charged-current absorption rates on free nucleons we do not implement any nucleon potentials other than the neutron–proton rest mass difference. For scattering on heavy nuclei, we use the [6] rate, include ion–ion correlations via [23], and a correction for the nuclear form factor via [24, 25]. For electron neutrino absorption on nuclei and inelastic neutrino-electron scattering, we implement the rates of [6]. For pair-processes, we implement both electron–positron annihilation via [6] and nucleon–nucleon Bremsstrahlung via [26].

¹⁸ We have included this progenitor model as part of the data release associated with this article. We note that this particular model has the following reference simulation: sollo03/s20/s20#presn and is also available at http://2sn.org/sollo03/s20@presn.gz.

We use three-neutrino species: ν_e , $\bar{\nu}_e$, and $\nu_x = \{\nu_\mu, \bar{\nu}_\mu, \nu_\tau, \text{ and } \bar{\nu}_\tau\}$. The SFHo EOS contains light clusters (²H, ³H, and ³He). While an approximation, all neutrino interactions (both scattering and absorption) on these light clusters are ignored. We do not reclassify the light clusters as either neutrons and protons, as alpha particles, or as heavy nuclei.

3. Contributions

In the following we briefly describe each of the simulation codes used in this comparison. We present details of the grid setup, the methods for solving the hydrodynamics, the methods and details of the radiation transport including the energy grid structure and any approximations and/or assumptions made. Each individual group also specifically mentions aspects of their simulation that deviates from the initial conditions and input physics as described in section 2.

3.1. 3DnSNe-IDSA

Contributors: Tomoya Takiwaki, Kei Kotake

3DnSNe is designed to solve one-(1D), two-(2D), and three-(3D) dimensional hydrodynamics problem in spherical geometry. A piecewise linear method with the geometrical correction of the spherical coordinates is used to reconstruct variables at the cell edge, where a modified van Leer limiter is employed to satisfy the condition of total variation diminishing (TVD) [27]. The numerical flux is calculated by a HLLC solver [28]. The computational grid is comprised of 512 logarithmically spaced, radial zones that cover from the center up to the outer boundary of 10^9 cm. The radial grid is chosen such that the resolution Δr is better than 250 m in the PNS star interior and typically better than 1 km outside the PNS. Though the previous works of this code are performed in Newtonian gravity [29–31], the effect of the GR potential is included in this run using Case A of [21].

Spectral neutrino transport is solved by the isotropic diffusion source approximation (IDSA) [32]. While only two species of neutrinos (electron neutrinos and electron antineutrinos) are included in this scheme in the original version, recently this scheme is extended to treat heavy-lepton neutrinos [33, 34]. In the formalism, the distribution function of the neutrinos is decomposed into a trapped part and a streaming part. The trapped part is once integrated and transported by the hydrodynamic equations. Then its spectrum is reconstructed to satisfy a Fermi–Dirac distribution. The free streaming neutrinos propagate with the characteristic speed following the closure relation [30]. In this run, 20 energy groups that logarithmically spread from 1 to 300 MeV are employed. The velocity-dependent terms $(\mathcal{O}(\frac{v}{c}))$ are only included (up to the leading order) in the trapped part of the distribution function (equation (15) in [32]). Nucleon–nucleon bremsstrahlung, electron–positron annihilation, and neutrino-electron scattering are included, as described in [33]. Following [16, 25], GR effects (time dilation) are approximately taken into account (see equations (1)–(6) in [33]). However, gravitational redshifting of the neutrino energies as they leave the gravitational well is not.

3.2. AGILE-BOLTZTRAN

Contributors: Tobias Fischer, Eric Lentz, Matthias Liebendörfer, Bronson Messer, Anthony Mezzacappa The radiation-hydrodynamics module AGILE is based on the spherically-symmetric and non-stationary metric of [35] and [36]. With the choice of orthogonal comoving spacetime coordinates, the equations of hydrodynamics in the presence of the neutrinoradiation field are given in [37] and [38]. They are solved by implicit conservative finite-differencing, with the implementation of a dynamically moving adaptive mass grid following

[39] and [40], allowing for the dynamical allocation of computational zones to regions where they are needed, which ensures an accurate shock capture [41, 42]. The energy dissipation in the presence of a shock front is considered via artificial viscosity based on the tensor viscosity formalism of [43]. In [44] AGILE has been upgraded to the second-order TVD advection scheme based on a Van Leer flux limiter. AGILE employs a flexible EOS module that has been implemented in [45] for the three independent variables temperature, rest-mass density and electron fraction. Contributions from electrons, positrons as well as photons are taken into account following the routines provided by [46] and [47].

The shock capturing properties of AGILE are key to its use in the core-collapse problem, but the grid reallocation that enables this does have another effect. The motion of zone boundaries in the AGILE scheme produces an effective advection that is essentially second-order in space with a correction term [41]. The correction term is everywhere present and depends on the grid spacing and the effective grid velocity (with respect to the matter). This induced numerical diffusivity is effective at smoothing initially sharp features in the flow, e.g. discontinuities introduced by burning processes during the late stages of massive star evolution. This effect will be directly responsible for some of the accretion-dependent differences we report in section 4.

The neutrino-transport module BOLTZTRAN consists of a GR time-implicit discreteangle (S_N) multi-species Boltzmann solver. BOLTZTRAN is coupled in an operator-split fashion to the hydrodynamics module AGILE, employing a direct finite-difference representation of the Boltzmann equation [5, 38, 41, 48, 49]. It solves for the neutrino distribution function, which depends on the spacetime coordinates as well as on the momentum coordinates propagation angle, relative to the radial direction, and neutrino energy. The treatment of inelastic neutrino-lepton scattering has been implemented in [4, 50]. Neutrinos in specific angle- and energy bins are created and destroyed according to the collisions. Freely-propagating neutrinos move along light-like geodesics between collisions, which gives rise to many correction terms in the Boltzmann equation due to the use of spherical coordinates in combination with a description of the neutrino phase space in a comoving frame [38, 44]. The finite-difference representation is upward compatible with limiting cases of the Boltzmann equation, e.g., the diffusion limit [51], and conserving total energy and lepton number.

The present core-collapse supernova runs are performed with 205 adaptive spatial zones. Solutions of the Boltzmann equation are resolved with 24 energy groups, geometrically increasing following the setup of [5], the first one centered at 0.5 MeV and the last at 300 MeV. The propagation angle has been discretized with six bins suitable for Gaussian quadrature.

The AGILE-BOLTZTRAN simulation in this paper deviates from the prescribed plan in the following ways. For the EOS, the SFHo nuclear EOS is only used above $T \simeq 0.45$ MeV. Below this temperature, for the present study we consider a low-density EOS with only one nucleus ²⁸Si. There is no nuclear burning of this nucleus to NSE at the transition temperature. In addition, we evolve four $(\nu_e, \bar{\nu}_e, \nu_x = \{\nu_\mu, \nu_\tau\}, \bar{\nu}_x = \{\bar{\nu}_\mu, \bar{\nu}_\tau\})$, instead of the prescribed three, neutrino species. For the plots below, we average the ν_x and $\bar{\nu}_x$ values. Also, we have included neutrino-positron inelastic scattering and extend our domain to 10^{10} cm, though we expect little impact from these particular deviations.

3.3. FLASH-M1

Contributors: Evan O'Connor, Sean Couch

FLASH [52, 53] is an open-source framework for hydrodynamic simulations of astrophysical environments, including core-collapse supernovae. Recently [16] have implemented both a GR effective potential [21] and a two-moment, energy-dependent neutrino transport scheme into FLASH following closely the implementation of [54] (also see the code description for GR1D below). For this work we use FLASH's unsplit hydrodynamics solver with piecewise parabolic method (PPM) reconstruction and the hybrid HLLC Riemann solver which reduces to HLLE in the presence of shocks. Our computational grid uses an adaptive mesh. We have a total of nine levels of refinement, on the coarsest level we have 160 grid zones extending from the origin to 10^9 cm. The grid zones on the finest level are \sim 244 m. We limit the maximum refinement so as to maintain at least $\Delta r/r \sim 0.009$ resolution. One improvement over [16] was triggered by this comparison work. We found that triggering mesh refinement based on entropy gradients (in addition to density and pressure) was important to maintain the sharpness of the density gradients near the compositional interfaces. We use 18 neutrino energy groups, spaced logarithmically from 1 to ~275 MeV. For the neutrino transport (also see section 3.5 below), the moment equations are solved in the coordinate frame. We solve the spatial fluxes and the energy-space fluxes explicitly, and the neutrino-matter interactions implicitly. We retain the full velocity dependence of the moment equations, except for the diffusion limit spatial fluxes, which are approximated to $\mathcal{O}(v/c)$. The explicit flux calculation localizes the solution to each zone (and its neighbors), and avoids expensive matrix solves.

Our treatment of pair-processes follows that of GR1D (see section 3.5 below). For this comparison we do not include neutrino-electron inelastic scattering. Due to its importance during the collapse phase, we start our FLASH-M1 simulations from 15 ms after core bounce using a model generated with GR1D (but instead of using full GR we use the GR effective potential to ensure a smooth and self-consistent mapping between the codes).

3.4. FORNAX

Contributors: Adam Burrows, David Vartanyan

FORNAX [55–57, 18, 58] is a multidimensional, multi-group radiation/hydrodynamic code employing a directionally-unsplit Godunov-type finite-volume TVD-limited reconstruction method, written in a covariant/coordinate-independent fashion, with generalized connection coefficients and static mesh refinement. It solves the comoving frame, multi-group, two-moment, velocity-dependent transport equations with an explicit Godunov characteristic method applied to the radiation transport operators and an implicit solver for the radiation source terms, uses the M1 tensor closure for the second and third moments of the radiation fields [59], and employs approximate general-relativistic gravity [21].

In FORNAX, by addressing the transport operator with an explicit method, we significantly reduce the computational complexity and communication overhead of traditional multidimensional radiative transfer solutions by bypassing the need for global iterative solvers that have proven to be slow and/or problematic beyond $\sim 10\,000$ cores. Radiation quantities are reconstructed with linear profiles, and the calculated edge states are used to determine fluxes via an HLLE solver. In the non-hyperbolic regime, the HLLE fluxes are corrected to reduce numerical diffusion [60].

For these comparison studies in 1D, the FORNAX run employs 16 energy groups for each of three species: ν_e , $\bar{\nu}_e$, and ν_x , where the latter subsumes the four known non-electron species. For the ν_e s, the energy range is 1 to 300 MeV, spaced logarithmically, and for the other two it is 1 to 100 MeV, also spaced logarithmically. The radial grid is logarithmic from \sim 100 km to the outer boundary and linear interior to \sim 100 km, with a central zone width of 0.5 km. The total number of radial zones is 608. Neutrino sources and sinks due to nucleon–nucleon

bremsstrahlung and electron–positron annihilation are included, as described in [61–63]. Neutrino-electron scattering is based on [6] as implemented in [64].

We deviate from the prescribed plan as follows, in FORNAX, we use corrections to the neutrino-heavy nuclei scattering cross section based on [63] and nucleon–nucleon brems-strahlung via [61]. Our computational grid extends to 2×10^9 cm.

3.5. GR1D

Contributors: Evan O'Connor

GR1D [54, 65] is an open-source, spherically-symmetric core-collapse supernova code. GR1D is fully GR. It uses the radial gauge, polar slicing metric of [65–67]. The hydrodynamics are solved via a second-order Runge-Kutta time stepping with third order spatial reconstruction via the PPM. We couple the neutrinos operator-split from the hydrodynamics. The neutrino transport is done via an energy-dependent M1 scheme where both the zeroth (energy density) and first (momentum density) angular moments of the neutrino distribution function are evolved [54, 68, 69]. The moment evolution equations are closed via an analytic closure that interpolates between the optically thick and optically thin limits of the Eddington factor using the expression from [70]. The scheme is fully GR and fully velocity dependent, except in the optically thick limit where the flux of the neutrino moments through cell boundaries is only computed to $\mathcal{O}(v/c)$. The spatial fluxes as well as the energy-space fluxes are computed explicitly, while the neutrino-matter interactions are handled implicitly. The time step is set by the light crossing time of the smallest zone and a Courant-Friedrichs-Lewy factor, which is taken to be 0.5 at all times except for near bounce, when 0.25 is used. For the simulations presented here, GR1D uses 18 energy groups, spaced logarithmically from 1 to 275 MeV. The spatial grid uses a constant spaced zoning of 300 m within the inner 20 km and outside 20 km the zoning increases logarithmically until a radius of $\sim 4 \times 10^9$ cm. There are 600 zones in total.

GR1D deviates from the prescribed plan in the following way. Our treatment of pair-processes, like electron-positron annihilation and nucleon-nucleon Bremsstrahlung are treated in an approximate way. First, we do not include thermal processes for electron neutrinos or antineutrinos. Second, for heavy-lepton neutrinos we do not fully solve the nonlinear neutrino-matter interaction terms Rather, we determine the emissivity of these processes assuming no final state neutrino blocking (via [63]). We then derive an effective absorption opacity using Kirchoff's law. This approximation is tested in [54]. Unlike the prescribed plan, our domain extends to $\sim 4 \times 10^9$ cm.

3.6. PROMETHEUS-VERTEX

Contributors: Robert Bollig, Hans-Thomas Janka

For the integration of the equations of hydrodynamics, PROMETHEUS-VERTEX employs the Newtonian finite-volume hydrodynamics code PROMETHEUS developed by [71]. PROMETHEUS is a direct Eulerian, time-explicit implementation of the PPM of [72], which is a second-order Godunov scheme based on a Riemann solver. PROMETHEUS is particularly well suited for following discontinuities in the fluid flow like shocks or boundaries between layers of different chemical composition by the help of a contact-steepening technique. Instead of a Newtonian gravitational potential the effective relativistic potential, Case A, of [21] is used, adopting the improved energy-conserving implementation of [73]. The consistent multifluid advection method of [74] is applied to ensure accurate advection of the individual chemical components of the fluid.

The VERTEX transport module consists of a time-implicit, conservative integrator of the three-species, energy-dependent moment equations of neutrino energy and momentum. It allows to simultaneously conserve energy and lepton number with good accuracy using the scheme described in [73]. The neutrino radiation quantities are computed in the comoving frame of the stellar fluid to order v/c. Corrections for GR gravitational redshift and time dilation are included. The closure relation for the two-moment set of equations is obtained in the form of a variable Eddington factor (connected to the radiation pressure) and a next-higher-order moment of neutrino radiation intensity, both of which are derived from the solutions of model-Boltzmann equations for all energy bins. The Boltzmann transport equation is simplified with respect to (numerically cumbersome) angular derivatives and integrated in radius-angle space on a tangent-ray mesh. The solutions of the Boltzmann problem and of the two-moment equations are iterated for convergence. Details of this transport code and its coupling to the hydrodynamics solver can be found in [25, 75].

The presented stellar collapse simulations were performed with a geometrical grid of 15 energy bins between 0 and 380 MeV for the boundary of the highest energy bin. The radial grid was contracted with the infalling flow up to core bounce and kept spatially fixed at later times. Initially, the grid contained 400 zones with variable radial spacing chosen such that $\Delta r/r < 0.028$ (except close to the center, where the central zone had a radius of ~ 0.233 km). During the simulation the grid was gradually refined in steps such that regions of steep density gradients in the near-surface layer of the PNS were resolved always with at least 20 radial cells per decade of density.

Unlike the prescribed plan, we have included neutrino-positron inelastic scattering, we do not expect an impact from this.

4. Results

In this section we present the results of our comparison. We begin with comparing hydrodynamic quantities and then discuss neutrino related quantities. Throughout all plots we use the following line style scheme, results from 3DnSNe-IDSA are shown in green, AGILE-BOLTZTRAN results are shown in black, FLASH results are shown in red, Fornax results are in blue, GR1D results are in gray, and PROMETHEUS-VERTEX results are shown in orange. All results are individually time-shifted so that bounce occurs at t = 0. For references, the individual collapse times (time from when the simulation starts to bounce) are ~275 ms (3DnSNe-IDSA), ~419 ms (AGILE-BOLTZTRAN), ~299.5 ms (FORNAX), ~298.2 ms (GR1D), ~297.8 ms (PROMETHEUS-VERTEX). All the data presented in this section is available, along with the scripts used to generate the figures. (Please see the supplementary data, available online at stacks.iop.org/jpg/45/104001/mmedia, for more information.)

In figure 1 we show the mass accretion rate, $\dot{M} = -4\pi R^2 \rho v$, measured at 500 km. Since the accretion on to the shock in the postbounce phase is supersonic, no hydrodynamic information can influence this quantity. Instead, it is mainly affected by the gravitational field, the initial collapse dynamics (before the infall becomes supersonic), and the low-density EOS. To mitigate differences, all codes, unless otherwise stated above, utilize the same low-density EOS [20], SFHo;, map the initial progenitor star via the same prescription (via interpolating density, temperature, and electron fraction), and use GR gravity (or an effective GR gravity). At a postbounce time of ~220 ms, the silicon–oxygen interface is accreted past 500 km and results in a steep drop of the mass accretion rate. We show a zoomed view of this region in the inset of figure 1. This interface, located at a baryonic mass coordinate of ~1.82 M_{\odot} , has an initial (at the onset of collapse) density contrast ($[\rho_{high} - \rho_{low}]/\rho_{high}$) of ~40%. The various

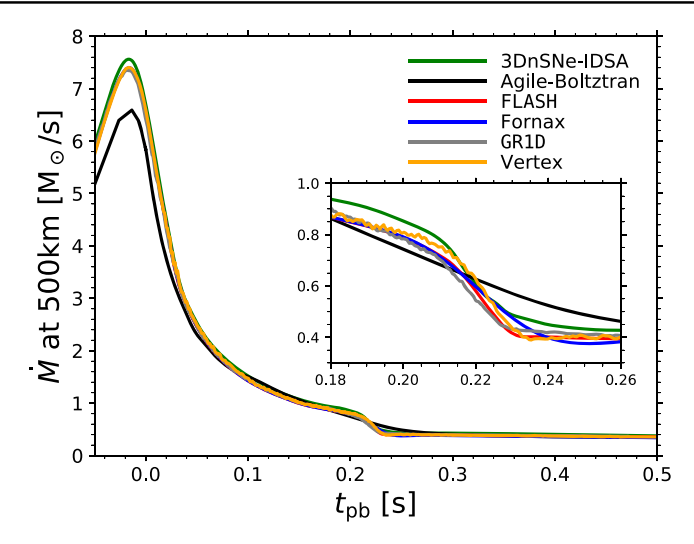


Figure 1. Mass accretion rate measured at 500 km as a function of postbounce time. We show in the inset a zoomed in plot of the mass accretion rate near the time when the silicon–oxygen interface accretes through 500 km. This gives a significant and steep drop in the mass accretion rate. All simulation codes predict a similar postbounce time for this interface accretion.

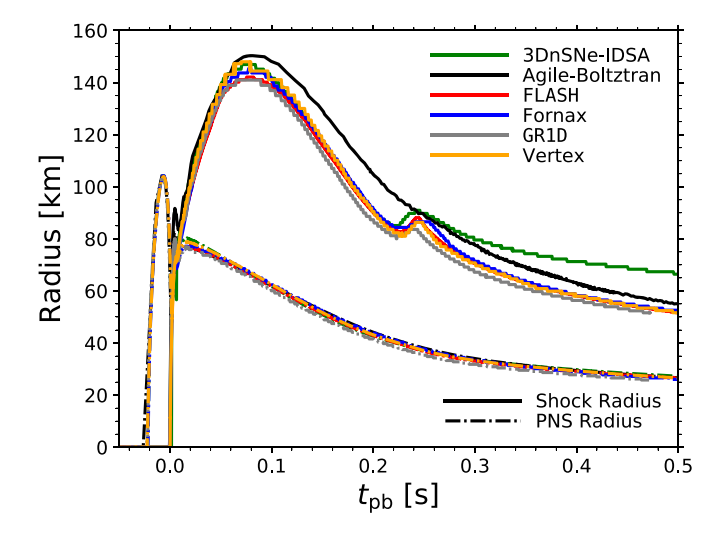


Figure 2. Shock radius (solid) and PNS radius (dashed) evolution as a function of postbounce time for each simulation in the comparison. The PNS radius is defined as the radial location with a density of 10^{11} g cm⁻³, which is why it is non-zero before bounce, while the shock radius is defined as the radius where the velocity is maximally negative. In AGILE-BOLTZTRAN the shock front spans a large radial range, here we take the radius where the velocity has dropped to half its peak value rather than the radius of the maximally negative value.

hydrodynamic codes maintain the steepness of this density gradient to varying degrees. Regarding the smoothness of the AGILE-BOLTZTRAN result, we remind the reader of the discussion in section 3.2 regarding the induced numerical diffusivity near sharp features in the

flow. While of small significance in spherical symmetry, this may play a larger role when comparing multidimensional simulations of core-collapse supernovae.

The next hydrodynamic quantity we compare is the shock radius. We show this comparison in figure 2. The shock forms very close to core bounce and initially travels out into the still infalling iron core. Due to energy losses from nuclear dissociation and neutrino emission, the shock slows, stalls, and begins to recede. In spherically-symmetric simulations of this progenitor, we do not expect shock revival. The codes compare quite well. The maximum radius reached by the supernova shock is between ~141 km (GR1D/FLASH) and ~150 km (AGILE-BOLTZTRAN). The time when the shock reaches its peak values ranges from ~74 ms (Vertex) to ~81 ms (AGILE-BOLTZTRAN). The shock continues to recede until the silicon—oxygen interface reaches the shock. At this time the mass accretion rate, and therefore the ram pressure, of the material above the shock decreases. All simulations (except AGILE-BOLTZTRAN) show a transient shock expansion at this time. The extent of the shock expansion depends on the steepness of the drop in the mass accretion rate (see figure 1). The adaptive Lagrangian grid of AGILE-BOLTZTRAN smooths out the silicon—oxygen interface and erases this feature. During the late stages, following the accretion of the silicon—oxygen interface we see a range of shock radius recession rates.

Related to the shock radius is the PNS radius. We take, as a definition of the PNS radius, the radius where the matter density $\rho=10^{11}\,\mathrm{g}\,\mathrm{cm}^{-3}$. We also show this radius in figure 2, all simulations predict a very similar PNS radius, including before bounce where this quantity simply denotes the radial location of the $\rho=10^{11}\,\mathrm{g}\,\mathrm{cm}^{-3}$ contour. We note the hierarchy of the PNS radius is generally related to the hierarchy of the shock radius [76]. GR1D has the smallest PNS radius and the smallest shock radius.

It is worth mentioning that AGILE-BOLTZTRAN and GR1D are the only true GR codes, the remaining codes use an effective potential to mimic GR effects. Despite this, the agreement across all of the codes, with no obvious systematic offsets between the true GR and effective GR codes, suggests that the GR effective potential does a remarkable job at capturing the relativistic dynamics, at least in spherical symmetry. Nevertheless, one should be cautious when using such an effective potential. There is one noteworthy, yet subtle, systematic difference between the full GR codes and the effective GR codes that is worth mentioning. Within the first ~5 ms of core bounce, the behavior of the PNS radius, the shock radius, and heavy-lepton neutrino luminosity (see below) shows an interesting feature in both AGILE-BOLTZTRAN and GR1D that is not present in the codes based on Newtonian hydrodynamics. Immediately following bounce, there is a faster expansion of these radii, and an additional local maximum that does not occur in the Newtonian runs. This does not appear to impact the subsequent dynamics.

We now focus our attention on comparing neutrino related quantities. The neutrino field plays a critical role in core-collapse supernovae. In the neutrino mechanism, the neutrinos are responsible for heating the matter and driving convection, both of which are crucial for ultimately launching the explosion. The neutrino heating is very sensitive to, and nonlinearly depends on, the properties of the neutrino field. Here we compare the neutrino luminosities, neutrino average energies, and also the total heating in the gain region. With this comparison we hope to show the variations one expects from various neutrino transport methods, the impact on the neutrino heating, and the excellent agreement between the various codes. Due to the varying definitions of the evolved neutrino variables, both the neutrino luminosities and neutrino average energies are transformed into a frame that is at rest (with respect to infinity). We report the luminosities and energies extracted from a sphere located at 500 km from the origin.

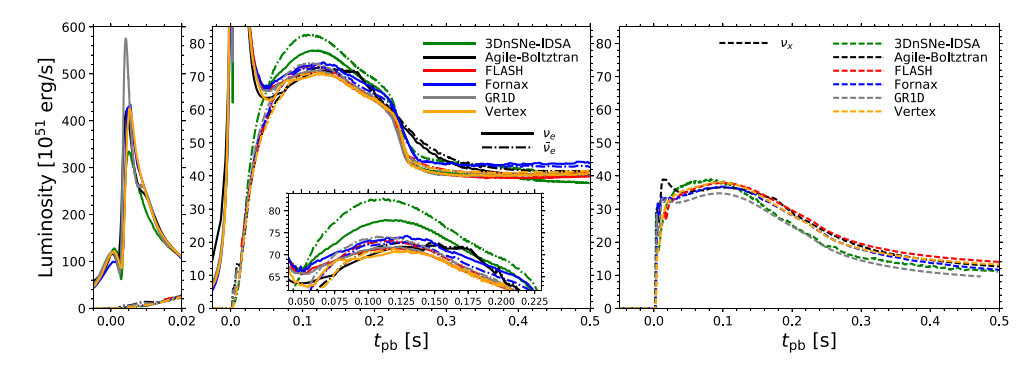


Figure 3. Neutrino luminosities as a function of postbounce time. In the left panels we show electron-type neutrino luminosities (solid lines show electron neutrinos while dashed—dotted lines show electron antineutrinos) and in the right panel we show the characteristic heavy-lepton neutrino luminosity (dashed line). For clarity, we show an inset to highlight the early accretion epoch for the electron-type neutrinos and a panel to show the neutronization burst. Some curves have been smoothed with neighboring zones to remove noise and improve clarity.

In figure 3 we show the electron neutrino (solid lines) and antineutrino (dashed–dotted lines) luminosities in the left two panels and the characteristic heavy-lepton neutrino luminosity (dashed lines; for a single species) in the right panel. For clarity, on the left we show both the neutronization peak, scaled out (leftmost panel) and an inset of the early accretion phase where the neutrino luminosity plateaus. We see variations among the codes for the height and shape of the neutronization burst which shows the sensitivity to the details of the neutrino transport (i.e. closure, treatment of electron scattering and neutrino–antineutrino pair- processes, and grid resolution to name a few). Within a single code, this feature is robustly universal across progenitor models [55, 60, 77]. During the accretion phase, 3DnSNe-IDSA predicts \sim 10% higher electron neutrino and antineutrino luminosities when compared to the other codes. These other codes compare well. During the early accretion phase (\sim 75 \sim 200 ms), the luminosities predicted between these codes vary by at most \sim 3B/s (\sim 5%) for electron neutrinos and electron antineutrinos. Most of the codes predict a slightly higher $\bar{\nu}_e$ luminosity starting at \sim 50–75 ms and continuing through to 500 ms.

The electron-type luminosities are mainly fuelled by accretion, therefore when the accretion rate drops around $\sim\!220$ ms, the electron-type luminosities have a corresponding drop. The roughly constant mass accretion rate following this time is responsible for the flat electron-type luminosities. After the silicon-oxygen interface accretes and the luminosities plateau again, we find variations of at most $\sim\!5$ B/s ($\sim\!12\%$). As a result of the smoothed mass accretion rate in figure 1 for the AGILE-BOLTZTRAN simulation, the drop at $\sim\!220$ ms is not as sharp as the other codes. The heavy-lepton neutrino luminosities show the largest discrepancy among the codes. The largest absolute difference between any two codes is $\sim\!6$ B/s at 400 ms, which, due to the low absolute luminosity, is upwards of 50%.

In addition to the neutrino luminosities, we show the neutrino average energies in figure 4. The average energies are computed by weighting the neutrino energies by the neutrino number spectrum. In the left panel we show electron neutrino (solid lines) and electron antineutrino (dashed–dotted lines) average energies while in the right panel we show the characteristic heavy-lepton neutrino average energies (dashed lines). Note, the scales are different. In all simulations we see common features. The electron neutrino average energies peak at bounce and then reach a minimum around ~45 ms after bounce. They then rise, at a

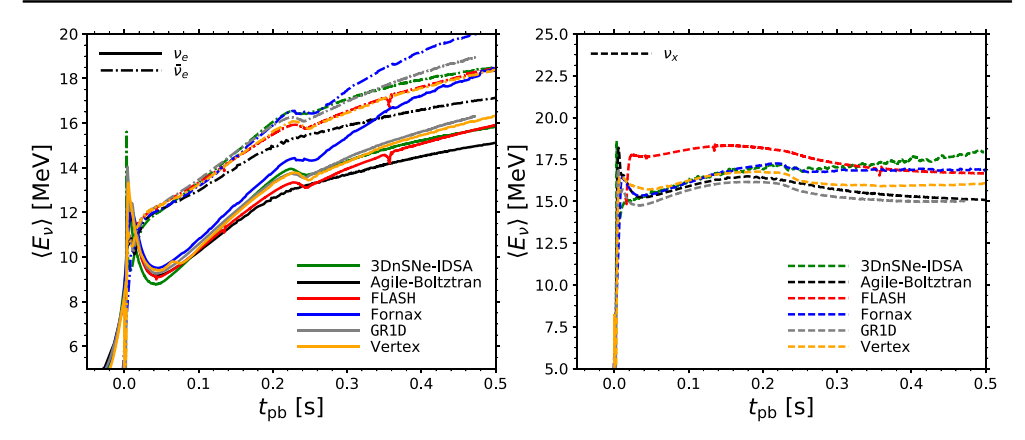


Figure 4. Neutrino average energy as a function of postbounce time. In the left panel we show electron-type neutrino average energies (solid lines show electron neutrinos while dashed—dotted lines show electron antineutrinos) and in the right panel we show the characteristic heavy-lepton neutrino average energy (dashed line). Some curves have been smoothed with neighboring zones to remove noise and improve clarity.

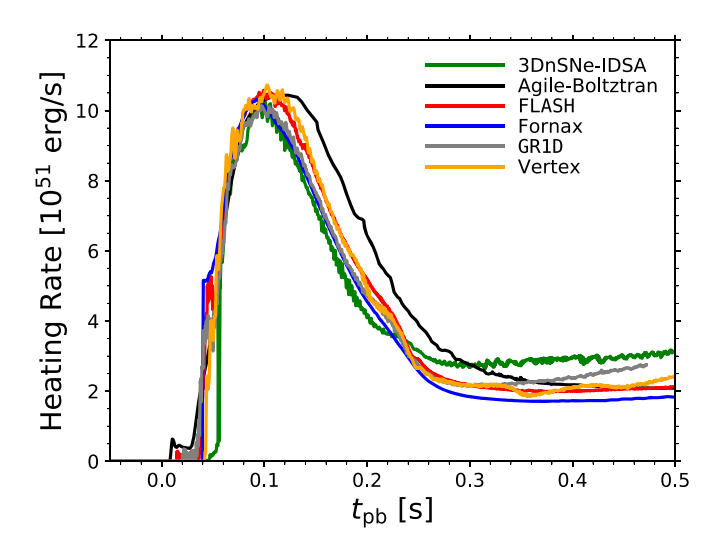


Figure 5. Neutrino heating in the gain region as a function of postbounce time. We define the neutrino heating to be the change in the internal energy of the matter due to the interaction with neutrinos. We only include contributions to the heating where there is a net transfer of energy to the matter from the neutrinos. In some simulations we place further cuts on the data to isolate the gain region, including $\rho < 3 \times 10^{10}$ g cm⁻³ and $s > 6 k_B/\text{baryon}$. Some curves have been smoothed with neighboring zones to remove noise and improve clarity.

similar rate as the electron antineutrinos, until the silicon–oxygen interface accretes in around \sim 220 ms. After this, the rise of the mean energies slows. All codes agree well (\lesssim 8% for electron neutrinos and \lesssim 6% for antineutrinos) until \sim 200 ms, after this time we see a divergence. For the heavy-lepton neutrino energies we see good agreement. We note that the FLASH ν_x mean energy is higher, as expected, because neutrino-electron inelastic scattering is omitted in this comparison. Furthermore, the blips in the FLASH mean energies (both

electron-type and heavy-lepton-type) occur when the shock front passes a mesh-refinement boundary. At this time, the energy-space coupling terms, which depend on the spatial gradient of the velocity field (which is large at the shock), are adversely impacted by the jump in grid spacing.

Next, in figure 5, we look at the predicted neutrino heating rate in each simulation. We define this heating as the rate of energy deposition into the internal energy of the matter in zones where this net energy exchange is positive (i.e. neutrino heating in the gain region)¹⁹. This particular quantity is highly nonlinear in that it sensitively depends on the electron neutrino and antineutrino spectra (both the overall luminosity and also the detailed shape) impinging on the gain region from below as well as the radial structure of the gain region itself and the composition of the matter. With this understood, we find excellent agreement in the heating rates in all codes. The rise of neutrino heating begins around 40–50 ms after bounce. The peak values, $\sim 10 \text{ B/s}$ at 100 ms, are $\lesssim 5\%$ different from each other. The heating rate drops after this peak and levels out around $\sim 2-3 \text{ B/s}$ after 250 ms.

During the next Galactic core-collapse supernovae, many neutrino detectors on Earth will detect neutrinos. Detailed core-collapse supernova simulations are the only way to predict what this signal will be and will be critical in aiding neutrino experimentalists and theorists to decipher the detected signal and extract the underlying physics. As a final comparison, we use the neutrino signals produced by each simulation to determine an approximate rate of neutrino interactions in a Super-Kamiokande-like water-Cherenkov detector due to electron antineutrino capture on free protons from a core-collapse supernova located at a distance of 10 kpc from Earth from a massive star similar to this $20 M_{\odot}$ model. This prediction is a toy model. It does not include any neutrino oscillations, or a detailed cross section. Furthermore, it is not complete, it is only for the first 500 ms, and even then, the impact of removing the spherical symmetry restriction (for example, potentially allowing an explosion to occur) will significantly alter the signal in reality prior to 500 ms. Nevertheless, this allows a comparison between the codes. This approximate rate is shown in equation (6). The interaction rate depends on the number of targets (free protons) in the detector, the inverse beta-decay cross section (electron antineutrino capture on protons), and the electron antineutrino number flux and spectral shape at the detector. To a good approximation, the inverse beta-decay cross section over the range of energies of interest depends on the neutrino energy squared. This allows us to write the neutrino interaction rate as a function of the mean squared neutrino energy. We use the following formula for this estimation,

$$R \sim \sigma \frac{2}{18} \frac{M_{\text{det}}}{m_{\text{amu}}} \frac{L_{\bar{\nu}_{e}}/\langle E_{\bar{\nu}_{e}}\rangle}{4\pi D^{2}} \frac{\langle E_{\bar{\nu}_{e}}^{2}\rangle}{(m_{e}c^{2})^{2}}$$

$$\sim \frac{1.6}{\text{ms}} \left[\frac{M_{\text{det}}}{32 \text{ kT}} \right] \left[\frac{L_{\bar{\nu}_{e}}}{10^{52} \text{ erg s}^{-1}} \right] \left[\frac{15 \text{ MeV}}{\langle E_{\bar{\nu}_{e}}\rangle} \right] \left[\frac{\langle E_{\bar{\nu}_{e}}^{2}\rangle^{1/2}}{15 \text{ MeV}} \right]^{2} \left[\frac{10 \text{ kpc}}{D} \right]^{2}, \tag{1}$$

where $\sigma = G_F^2/(\hbar c)^4 \cos(\theta_C)^2 (m_e c^2)^2 (1+3g_A^2)/\pi \sim 2.5 \times 10^{-44} \, \mathrm{cm}^2$, is a reference cross section for absorption of neutrinos on to nucleons [63]; M_{det} is the detector mass, here taken to be the inner-volume mass of Super-Kamiokande, 32 kT [78]; $m_{\mathrm{amu}} = 1.66054 \times 10^{-24} \, \mathrm{g}$ is the atomic mass unit; D is the distance; and $L_{\bar{\nu}_e}$, $\langle E_{\bar{\nu}_e} \rangle$, and $\langle E_{\bar{\nu}_e}^2 \rangle$ are the electron antineutrino luminosity, mean energy, and mean squared energy, respectively. The mean energies are taken with respect to the neutrino number spectrum.

¹⁹ While included in the simulation, FORNAX does not include the energy exchanged from neutrino-electron scattering in this heating source term. We estimate from the other simulations that this would increase the heating by less than 5% at the peak and less than 10% at later times.

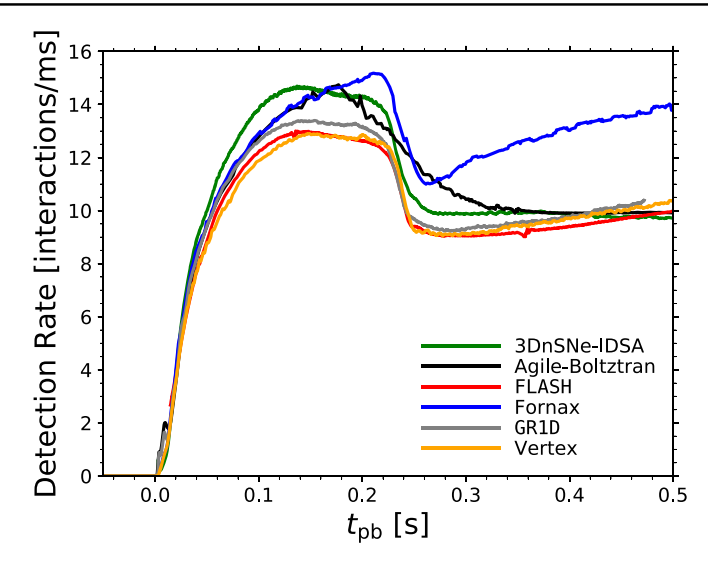


Figure 6. Approximate detection rate in a Super-Kamiokande-like water-Cherenkov detector for model supernovae (of a $20\,M_\odot$ progenitor at $10\,\mathrm{kpc}$ based on equation (1)). This prediction does not take into account neutrino oscillations. It is meant to demonstrate a typical systematic uncertainty for neutrino detection rate predictions.

We show the resulting approximate detection rate calculated from each simulation in figure 6. The initial rise follows the shape of the electron antineutrino signal, it reaches a peak value of $\sim \! 14$ interactions/ms after $\sim \! 100$ ms. Similar to the neutrino heating, the approximate detection rate is very sensitive to the neutrino spectra. We see good agreement, especially at early times between all of the simulations. The largest variation in the detection rate at 100 ms is $\sim \! 15\%$. At later times, the deviation in the neutrino energies (and, in particular, also in the mean squared energies; not shown) seen in figure 4 causes a deviation in the approximate detection rate upwards of 40%.

5. Discussion and summary

The goal of this work was to bring together groups of researchers studying core-collapse supernovae and collaboratively work together to perform a global comparison between simulation codes. As we progress forward with multidimensional simulations and begin to successfully model supernovae, it is worth taking the time and effort to convince ourselves, and others, that on a basic and fundamental level, we find broad agreement across independent codes and physics implementations. With this effort we have taken the first steps toward this goal with the first extensive code-to-code comparison in over 10 years, between six core-collapse supernova codes: 3DnSNe-IDSA, AGILE-BOLTZTRAN, FLASH (with its M1 neutrino transport implementation), FORNAX, GR1D, and PROMETHEUS-VERTEX. We have developed a comprehensive and strict set of initial conditions and input neutrino-and nuclear-physics in order to eliminate as many sources of potential differences between our various simulation codes. Our goal with this comparison is not to search for and explain any and all differences we find between our various codes (although this has occurred to some extent), or to make statements about which code is more trustworthy than the others. Rather, it is to provide a reference for each other, new researchers to the field, and the external audience

on the state of agreement between core-collapse supernova simulation codes. This is in part because in many aspects it is unclear what the correct answer is. Furthermore, where differences do arise, they may be simply due to various numerical approximations, such as the neutrino transport methods or the hydrodynamics methods, or the numerical implementation of the microphysics. Removing all these differences would be difficult, and even undesirable, as we ideally want to compare the production versions of the various codes. Indeed, it has not been the main goal of the community to drive the convergence of the spherically symmetric case below few percent deviations, which very well could be possible with enough effort. Rather, the ultimate goal in the community is to develop codes that work in multi-D, model core-collapse supernovae as realistically as possible, and show similar convergence.

We have compared select, but critical, aspects from these six codes using sphericallysymmetric simulations of the core-collapse and the early postbounce phase (first 500 ms) of a core-collapse supernova of a $20 M_{\odot}$ star. These include the mass accretion rate on to the PNS, the shock radius and PNS radius evolution, the neutrino luminosity and mean energy of each of the three-neutrino species included, and the neutrino heating in the gain region. The mass accretion rates are mostly a test of the low-density EOS and gravity implementations, these agree well between the codes, especially after \sim 40 ms. The shock radius evolution shows good agreement across the codes across the window of time considered, especially, for most codes, during the phase when the interface between the silicon and oxygen shell passes the shock. There we see a transient shock expansion in most codes that all begin within ~ 10 ms of each other at a postbounce time of \sim 225 ms. With regard to the evolution of the PNS radius during the entire time window, the agreement across all of the codes considered is remarkable. The neutrino luminosity and mean energy also show good agreement. During the strongest accretion phase, between ~ 100 and ~ 200 ms, all of the reported electron-type neutrino luminosities (those that drive the neutrino heating) agree within \sim 15%, and most agree within $\sim 5\%$. The absolute difference in the heavy-lepton neutrino luminosity is similar to the electron-types, but the much lower value gives a larger relative variation, from $\sim 10\%$ in the accretion phase and growing upwards of \sim 50% at 500 ms. Regarding the neutrino mean energies, at early times they agree well, within \sim 5%, but the variation grows with time up to $\sim 25\%$ at late times. We do note that the evolution of some of our quantities—like the shock radii, neutrino luminosities, and neutrino energies-tend to show some divergence at later times for some of the codes. We have not diagnosed this difference here, but it useful to keep in mind going forward. The neutrino heating rate is a very nonlinear quantity and therefore it is useful to compare it amongst the codes. It is sensitive to the electron-type neutrino spectra (the overall luminosity, and the spectral shape) as well as the structure of the region just behind the shock front. We find noteworthy agreement of this quantity in our simulations. The peak heating rate at \sim 100 ms after bounce agrees between all the codes to better than \sim 5%. Finally, for each code, we made an approximate prediction for the interaction rate of electron antineutrinos in an Earth-based water-Cherenkov detector similar to the currently-running Super-Kamiokande. While we have left details out of this estimate (like neutrino oscillation effects, detailed cross sections, and detector efficiencies), this estimate is useful for determining a typical systematic error that one can associate with neutrino signal predictions from core-collapse codes. This error will vary depending on the detector type and the interaction channel, but such a detailed calculation is left to future work.

In the future, we hope to continue to achieve the agreement seen here while at the same time including more detailed and modern neutrino and nuclear physics, as well as extending our comparison to multiple dimensions. The growth and impact of multidimensional instabilities, such as convection and turbulence, is likely to depend more sensitively on the choice of hydrodynamic methods and grids. However, with this base set of comparisons we will have an excellent starting point for this future work.

Acknowledgments

EO would like to thank Almudena Arcones for co-guest editing this *Journal of Physics* G focus issue and for discussions on the design and goals of this comparison work.

3DnSNe-IDSA: KK and TT acknowledge support by the JSPS KAKENHI Grant Numbers (JP15H00789, JP15H01039, JP17H01130, JP17H06364, JP17K14306, JP17H05206, and JP18H01212), and by the Central Research Institute of Fukuoka University (Nos.171042, 177103), and by JICFuS which chose the code development of 3DnSNe-IDSA as a priority issue to be tackled by using the Post 'K' Computer.

Agile-Boltztran: TF acknowledges support by the Polish National Science Center (NCN) under grant number UMO-2016/23/B/ST2/00720. This work was supported by the COST Actions CA16117 'ChETEC' and CA16214 'PHAROS'. AM acknowledges support from the National Science Foundation (NSF GP 1505933). The Agile-Boltztran supernova simulations were performed at the Wroclaw Center for Supercomputing and Networking (WCSS).

FLASH & GR1D: EO acknowledges that partial support for this work was provided by NASA through Hubble Fellowship grant #51344.001-A awarded by the Space Telescope Science Institute, which is operated by the Association of Universities for Research in Astronomy, Inc., for NASA, under contract NAS 5-26555. SMC is supported by the US Department of Energy, Office of Science, Office of Nuclear Physics, under Award Numbers DE-SC0015904 and DE-SC0017955 and the Chandra x-ray Observatory under grant TM7-18005X. FLASH & GR1D computations were performed on resources provided by the Swedish National Infrastructure for Computing (SNIC) at the PDC Center for High Performance Computing (PDC).

Fornax: AB and DV employed computational resources for this study provided by the TIGRESS high performance computer center at Princeton University, which is jointly supported by the Princeton Institute for Computational Science and Engineering (PICSciE) and the Princeton University Office of Information Technology. AB acknowledges support under US NSF Grant AST-1714267 and the Max Planck/Princeton Center (MPPC) for Plasma Physics (NSF PHY-1144374), and by the DOE SciDAC4 Grant DE-SC0018297 (subaward 00009650).

Prometheus-Vertex: At Garching, this work was supported by the European Research Council through grant ERC AdG 341157-COCO2CASA, and by the Deutsche Forschungsgemeinschaft (DFG) through the Cluster of Excellence 'Universe' (EXC 153) and Sonderforschungsbereich 'Neutrinos and Dark Matter in Astro- and Particle Physics' (SFB 1258). Computational resources by the Max Planck Computing and Data Facility (MPCDF) are acknowledged.

Provided Data

Upon publication of this article we will provide all the finalized data used to make all of the figures in this article, including the plotting scripts. This consists of time series data for each simulation code for at least \dot{M} at 500 km, shock radius, PNS radius, 3 species (electron neutrino, electron antineutrino, and a characteristic heavy-lepton neutrino) neutrino luminosity, mean energy, and mean squared energy (in some cases we provide the pinching parameter α , which is analytically related to the mean squared energy), and the net heating rate in the gain region.

ORCID iDs

Evan O'Connor https://orcid.org/0000-0002-8228-796X David Vartanyan https://orcid.org/0000-0003-1938-9282

References

- May M M and White R H 1966 Hydrodynamic calculations of general-relativistic collapse *Phys. Rev.* 141 1232–41
- [2] Colgate S A and White R H 1966 The hydrodynamic behavior of supernovae explosions Astrophys. J. 143 626
- [3] Arnett W D 1966 Gravitational collapse and weak interactions Can. J. Phys. 44 2553-94
- [4] Mezzacappa A and Bruenn S W 1993 Stellar core collapse—a Boltzmann treatment of neutrinoelectron scattering Astrophys. J. 410 740
- [5] Mezzacappa A and Bruenn S W 1993 A numerical method for solving the neutrino Boltzmann equation coupled to spherically symmetric stellar core collapse Astrophys. J. 405 669
- [6] Bruenn S W 1985 Stellar core collapse—numerical model and infall epoch Astrophys. J. Suppl. Ser. 58 771
- [7] Yamada S, Janka H-T and Suzuki H 1999 Neutrino transport in type II supernovae: Boltzmann solver versus Monte Carlo method Astron. Astrophys. 344 533–50
- [8] Messer O E B, Mezzacappa A, Bruenn S W and Guidry M W 1998 A comparison of Boltzmann and multigroup flux-limited diffusion neutrino transport during the postbounce shock reheating phase in core-collapse supernovae Astrophys. J. 507 353–60
- [9] Ott C D, Burrows A, Dessart L and Livne E 2008 Two-dimensional multiangle multigroup neutrino radiation-hydrodynamic simulations of postbounce supernova cores Astrophys. J. 685 1069–88
- [10] Burrows A, Young T, Pinto P, Eastman R and Thompson T A 2000 A new algorithm for supernova neutrino transport and some applications Astrophys. J. 539 865–87
- [11] Richers S, Nagakura H, Ott C D, Dolence J, Sumiyoshi K and Yamada S 2017 A detailed comparison of multidimensional Boltzmann neutrino transport methods in core-collapse supernovae Astrophys. J. 847 133
- [12] Liebendorfer M, Rampp M, Janka H-T and Mezzacappa A 2005 Supernova simulations with Boltzmann neutrino transport: a comparison of methods Astrophys. J. 620 840–60
- [13] Just O, Bollig R, Janka H-T, Obergaulinger M, Glas R and Nagataki S 2018 Core-collapse supernova simulations in one and two dimensions: comparison of codes and approximations arXiv:1805.03953
- [14] Bruenn S W et al 2016 The development of explosions in axisymmetric Ab initio core-collapse supernova simulations of 12–25 msolar stars Astrophys. J. 818 123
- [15] Summa A, Hanke F, Janka H-T, Melson T, Marek A and Müller B 2016 Progenitor-dependent explosion dynamics in self-consistent axisymmetric simulations of neutrino-driven corecollapse supernovae Astrophys. J. 825 6
- [16] O'Connor E P and Couch S M 2018 Two-dimensional core-collapse supernova explosions aided by general relativity with multidimensional neutrino transport Astrophys. J. 854 63
- [17] Suwa Y, Yamada S, Takiwaki T and Kotake K 2015 The criterion of supernova explosion revisited: the mass accretion history Astrophys. J. 816 43
- [18] Vartanyan D, Burrows A, Radice D, Skinner M A and Dolence J 2018 Revival of the fittest: exploding core-collapse supernovae from 12 to 25 M_☉ Mon. Not. R. Astron. Soc. 477 3091–108
- [19] Woosley S and Heger A 2007 Nucleosynthesis and remnants in massive stars of solar metallicity Phys. Rep. 442 269–83
- [20] Steiner A W, Hempel M and Fischer T 2013 Core-collapse supernova equations of state based on neutron star observations Astrophys. J. 774 17
- [21] Marek A, Dimmelmeier H, Janka H-T, Müller E and Buras R 2006 Exploring the relativistic regime with newtonian hydrodynamics: an improved effective gravitational potential for supernova simulations Astron. Astrophys. 445 273–89
- [22] Horowitz C J 2002 Weak magnetism for antineutrinos in supernovae Phys. Rev. D 65 043001

- [23] Horowitz C J 1997 Neutrino trapping in a supernova and the screening of weak neutral currents Phys. Rev. D 55 4577–81
- [24] Bruenn S W and Mezzacappa A 1997 Ion screening effects and stellar collapse Phys. Rev. D 56 7529–47
- [25] Rampp M and Janka H-T 2002 Radiation hydrodynamics with neutrinos Astron. Astrophys. 396 361–92
- [26] Hannestad S and Raffelt G 1998 Supernova neutrino opacity from nucleon–nucleon bremsstrahlung and related processes Astrophys. J. 507 339–52
- [27] Mignone A 2014 High-order conservative reconstruction schemes for finite volume methods in cylindrical and spherical coordinates J. Comput. Phys. 270 784–814
- [28] Toro E F, Spruce M and Speares W 1994 Restoration of the contact surface in the HLL-Riemann solver Shock Waves 4 25–34
- [29] Takiwaki T, Kotake K and Suwa Y 2012 Three-dimensional hydrodynamic core-collapse supernova simulations for an 11.2 M_☉ star with spectral neutrino transport Astrophys. J. 749 98
- [30] Takiwaki T, Kotake K and Suwa Y 2014 A comparison of two- and three-dimensional neutrinohydrodynamics simulations of core-collapse supernovae Astrophys. J. 786 83
- [31] Takiwaki T, Kotake K and Suwa Y 2016 Three-dimensional simulations of rapidly rotating corecollapse supernovae: finding a neutrino-powered explosion aided by non-axisymmetric flows *Mon. Not. R. Astron. Soc.* 461 L112–6
- [32] Liebendrfer M, Whitehouse S C and Fischer T 2009 The isotropic diffusion source approximation for supernova neutrino transport Astrophys. J. 698 1174–90
- [33] Kotake K, Takiwaki T, Fischer T, Nakamura K and Martínez-Pinedo G 2018 Impact of neutrino opacities on core-collapse supernova simulations Astrophys. J. 853 170
- [34] Sotani H and Takiwaki T 2016 Gravitational wave asteroseismology with protoneutron stars *Phys. Rev.* D 94 044043
- [35] Misner C W and Sharp D H 1964 Relativistic equations for adiabatic, spherically symmetric gravitational collapse Phys. Rev. 136 571
- [36] May M M and White R H 1966 Hydrodynamic calculations of general-relativistic collapse Phys. Rev. 141 1232–41
- [37] Liebendörfer M, Mezzacappa A and Thielemann F-K 2001 Conservative general relativistic radiation hydrodynamics in spherical symmetry and comoving coordinates *Phys. Rev.* D 63 104003
- [38] Liebendörfer M et al 2004 A finite difference representation of neutrino radiation hydrodynamics for spherically symmetric general relativistic supernova simulations Astrophys. J. Suppl. Ser. 150 263–316
- [39] Winkler K-H A, Norman M L and Mihalas D 1984 Adaptive-mesh radiation hydrodynamics—I. The radiation transport equation in a completely adaptive coordinate system: II. The radiation and fluid equations in relativistic flows J. Quant. Spectrosc. Radiat. Transfer 31 473
- [40] Dorfi E A and Drury L O 1987 Simple adaptive grids for 1-D initial value problems J. Comput. Phys. 69 175
- [41] Liebendörfer M, Rosswog S and Thielemann F-K 2002 An adaptive grid, implicit code for spherically symmetric, general relativistic hydrodynamics in comoving coordinates Astrophys. J. Suppl. Ser. 141 229–46
- [42] Fischer T, Whitehouse S C, Mezzacappa A, Thielemann F-K and Liebendörfer M 2010 Protoneutron star evolution and the neutrino-driven wind in general relativistic neutrino radiation hydrodynamics simulations Astron. Astrophys. 517 A80
- [43] Tscharnuter W M and Winkler K-H A 1979 A method for computing selfgravitating gas flows with radiation Comput. Phys. Commun. 18 171
- [44] Liebendörfer M, Rampp M, Janka H-T and Mezzacappa A 2005 Supernova simulations with boltzmann neutrino transport: a comparison of methods Astrophys. J. 620 840–60
- [45] Hempel M, Fischer T, Schaffner-Bielich J and Liebendörfer M 2012 New equations of state in simulations of core-collapse supernovae Astrophys. J. 748 70
- [46] Timmes F X and Arnett D 1999 The accuracy, consistency, and speed of five equations of state for stellar hydrodynamics Astrophys. J. Suppl. Ser. 125 277
- [47] Timmes F X and Swesty F D 2000 The accuracy, consistency, and speed of an electron–positron equation of state based on table interpolation of the Helmholtz free energy Astrophys. J. Suppl. Ser. 126 501

- [48] Mezzacappa A and Bruenn S W 1993 Type II supernovae and Boltzmann neutrino transport—the infall phase Astrophys. J. 405 637–68
- [49] Mezzacappa A and Messer O E B 1999 Neutrino transport in core collapse supernovae J. Comput. Appl. Math. 109 281
- [50] Fischer T, Whitehouse S C, Mezzacappa A, Thielemann F-K and Liebendörfer M 2009 The neutrino signal from protoneutron star accretion and black hole formation Astron. Astrophys. 499 1
- [51] Liebendörfer M, Whitehouse S C and Fischer T 2009 The isotropic diffusion source approximation for supernova neutrino transport Astrophys. J. 698 1174
- [52] Fryxell B, Olson K, Ricker P, Timmes F X, Zingale M, Lamb D Q, MacNeice P, Rosner R, Truran J W and Tufo H 2000 FLASH: an adaptive mesh hydrodynamics code for modeling astrophysical thermonuclear flashes Astrophys. J. Suppl. Ser. 131 273–334
- [53] Couch S M and O'Connor E P 2014 High-resolution three-dimensional simulations of corecollapse supernovae in multiple progenitors Astrophys. J. 785 123
- [54] O'Connor E 2015 An open-source neutrino radiation hydrodynamics code for core-collapse supernovae Astrophys. J. Suppl. Ser. 219 24
- [55] Wallace J, Burrows A and Dolence J C 2016 Detecting the supernova breakout burst in terrestrial neutrino detectors Astrophys. J. 817 182
- [56] Skinner M A, Burrows A and Dolence J C 2016 Should one use the ray-by-ray approximation in core-collapse supernova simulations? Astrophys. J. 831 81
- [57] Burrows A, Vartanyan D, Dolence J C, Skinner M A and Radice D 2018 Crucial physical dependencies of the core-collapse supernova mechanism Space Sci. Rev. 214 33
- [58] Radice D, Burrows A, Vartanyan D, Skinner M A and Dolence J C 2017 Electron-capture and low-mass iron-core-collapse supernovae: new neutrino-radiation-hydrodynamics simulations Astrophys. J. 850 43
- [59] Vaytet N M H, Audit E, Dubroca B and Delahaye F 2011 A numerical model for multigroup radiation hydrodynamics J. Quant. Spectrosc. Radiat. Transfer 112 1323–35
- [60] O'Connor E and Ott C D 2013 The progenitor dependence of the pre-explosion neutrino emission in core-collapse supernovae Astrophys. J. 762 126
- [61] Thompson T A, Burrows A and Horvath J E 2000 μ and τ neutrino thermalization and production in supernovae: processes and time scales *Phys. Rev.* C 62 035802
- [62] Burrows A and Thompson T A 2004 Neutrino-matter interaction rates in supernovae Astrophysics and Space Science Library (Dordecht: Springer) pp 133-74
- [63] Burrows A, Reddy S and Thompson T A 2006 Neutrino opacities in nuclear matter Nucl. Phys. A 777 356–94
- [64] Thompson T A, Burrows A and Pinto P A 2003 Shock breakout in core-collapse supernovae and its neutrino signature Astrophys. J. 592 434–56
- [65] O'Connor E and Ott C D 2010 A new open-source code for spherically symmetric stellar collapse to neutron stars and black holes Class. Quantum Grav. 27 114103
- [66] Gourgoulhon E 1991 Simple equations for general relativistic hydrodynamics in spherical symmetry applied to neutron star collapse Astron. Astrophys. 252 651–63
- [67] Romero J V, Ibanez J M A, Marti J M A and Miralles J A 1996 A new spherically symmetric general relativistic hydrodynamical code Astrophys. J. 462 839
- [68] Shibata M, Kiuchi K, Sekiguchi Y I and Suwa Y 2011 Truncated moment formalism for radiation hydrodynamics in numerical relativity *Prog. Theor. Phys.* 125 1255–87
- [69] Cardall C Y, Endeve E and Mezzacappa A 2013 Conservative 3+1 general relativistic variable Eddington tensor radiation transport equations *Phys. Rev.* D 87 103004
- [70] Minerbo G N 1978 Maximum entropy eddington factors J. Quant. Spectrosc. Radiat. Transfer 20 541–5
- [71] Fryxell B, Müller E and Arnett W 1989 Hydrodynamics and Nuclear Burning Max Planck Institut für Astrophysik, Garching preprint MPA 449
- [72] Colella P and Woodward P R 1984 The piecewise parabolic method (PPM) for gas-dynamical simulations J. Comput. Phys. 54 174–201
- [73] Müller B, Janka H-T and Dimmelmeier H 2010 A new multi-dimensional general relativistic neutrino hydrodynamic code for core-collapse supernovae: I. Method and code tests in spherical symmetry Astrophys. J. Suppl. Ser. 189 104–33
- [74] Plewa T and Müller E 1999 The consistent multi-fluid advection method *Astron. Astrophys.* **342** 179–91

- [75] Buras R, Rampp M, Janka H-T and Kifonidis K 2006 Two-dimensional hydrodynamic corecollapse supernova simulations with spectral neutrino transport Astron. Astrophys. 447 1049–92
- [76] Janka H-T 2001 Conditions for shock revival by neutrino heating in core-collapse supernovae *Astron. Astrophys.* **368** 527–60
- [77] Kachelrieß M, Tomàs R, Buras R, Janka H-T, Marek A and Rampp M 2005 Exploiting the neutronization burst of a galactic supernova Phys. Rev. D 71 063003
- [78] Scholberg K 2012 Supernova neutrino detection Annu. Rev. Nucl. Part. Sci. 62 81-103